A&A 493, 1–11 (2009)
DOI: 10.1051/0004-6361:200811004

Astronomy & Astrophysics

Magnetic field effects on neutrino production in microquasars

M. M. Reynoso[1,2,⋆] and G. E. Romero[3,4,⋆⋆]

[1] Departamento de Física, Facultad de Ciencias Exactas y Naturales, Universidad Nacional de Mar del Plata, Funes 3350, (7600) Mar del Plata, Argentina
e-mail: mreynoso@mdp.edu.ar
[2] Instituto de Investigaciones Físicas de Mar del Plata, (UNMdP – CONICET), Argentina
[3] Instituto Argentino de Radioastronomía (CCT La Plata – CONICET), C.C.5, 1894 Villa Elisa, Buenos Aires, Argentina
[4] Facultad de Ciencias Astronómicas y Geofísicas, Universidad Nacional de La Plata, Paseo del Bosque s/n, 1900 La Plata, Argentina

Received 20 September 2008 / Accepted 14 October 2008

ABSTRACT

Aims. We investigate the effects of magnetic fields on neutrino production in microquasars.
Methods. We calculated the steady particle distributions for the pions and muons generated in $p\gamma$ and pp interactions in the jet taking the effects of all energy losses into account.
Results. The obtained neutrino emission is significantly modified due to the synchrotron losses suffered by secondary pions and muons.
Conclusions. The estimates made for neutrino fluxes arriving on the Earth imply that detection of high-energy neutrinos from the vicinity of the compact object can be difficult. However, in the case of windy microquasars, the interaction of energetic protons in the jet with matter of dense clumps of the wind could produce detectable neutrinos. This is because the pions and muons at larger distances from the compact object will not be affected by synchrotron losses.

Key words. X-rays: binaries – neutrinos – radiation mechanisms: non-thermal

1. Introduction

Microquasars, the X-ray binary systems with non-thermal jets, are considered important candidate sources of high-energy neutrinos (Waxman & Levinson 2001). The recent detection of TeV gamma rays reveals that these objects are capable of accelerating particles to very high energies (Aharonian et al. 2005; Albert et al. 2006; Albert et al. 2007). The models that predict both gamma ray and neutrino emission are based on interactions of relativistic protons in the jet with cold protons of a dense wind from a high-mass stellar companion (Romero et al. 2003; Christiansen et al. 2006), with secondary synchrotron emission in the jet itself (Romero & Vila 2008), and with cold protons in a heavy jet (Reynoso et al. 2008). A usual assumption made in these models is equipartition between the magnetic energy and the kinetic energy in the jets, which leads to large magnetic fields. In this work, we analyze the effects caused by the presence of such strong magnetic fields on the spectra of secondary particles that decay to neutrinos.

The outline of this work is as follows. In the next section we briefly discuss the basics of hadronic models for microquasars, and in Sect. 3 we deal with the acceleration and cooling mechanisms relevant to the primary relativistic particles in the jet. In Sect. 4, we analyze the effects of the magnetic field on the spectra of secondary pions, muons, and neutrinos. In Sect. 5, we discuss the neutrino production through interactions between the jet and clumps of the stellar wind in high-mass microquasars. The last two sections include a discussion of the results and a summary.

2. Basics of hadronic models of microquasars

In these models, an accretion disk is present around the compact object, and a fraction of the accreted material is expelled in two oppositely directed jets (Falcke & Biermann 1995). We assume conical jets with a half-opening angle ξ and radius $r(z) = z_0 \tan \xi$, where the injection point is at a distance z_0 from the compact object. A sketch of a high-mass microquasar is shown in Fig. 1, where the star presents a wind with a clumply structure. In the case of a low-mass microquasar, there is no significant stellar wind.

The kinetic luminosity of the jet, L_k, implies a kinetic energy density of

$$\rho_k(z) = \frac{L_k}{\pi r^2 v_b}, \quad (1)$$

where v_b is the bulk velocity of the jet particles. Following the jet-accretion coupling hypothesis, we assume that around 10% of the Eddington luminosity goes into the jet (Körding et al. 2006). We adopt $L_k = 10^{38}$ erg s^{-1} for a 10 $M_\odot$ black hole. Equipartition then implies a magnetic energy density $\rho_{mag} = \rho_k$, and hence a magnetic field (e.g. Bosch-Ramon et al. 2006)

$$B(z) = \sqrt{8\pi\rho_k(z)}. \quad (2)$$

We consider that a fraction of the kinetic power in the jet is carried by relativistic primary protons and electrons, $L_{rel} = L_p + L_e$.

⋆ Fellow of CONICET.
⋆⋆ Member of CONICET.

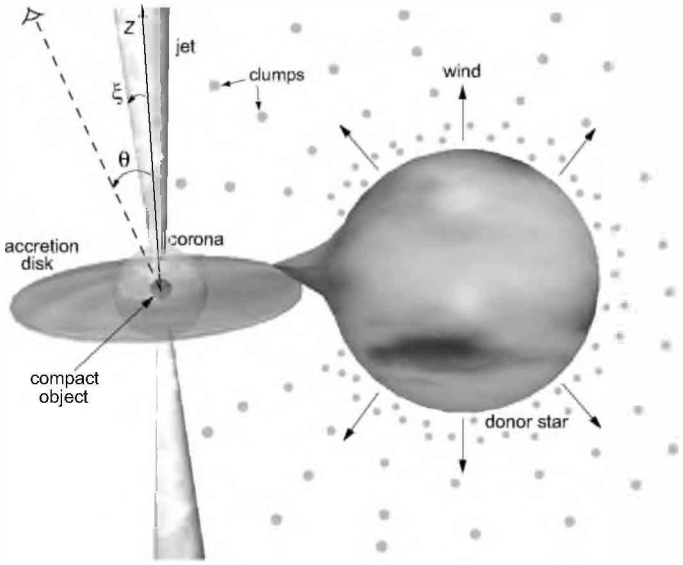

Fig. 1. Schematic view of a high-mass microquasar.

The relation between the proton and electron power is given by a certain parameter a in such a way that $L_p = a\,L_e$. This parameter is unknown, although there are reasons to think that $a > 1$. We consider the cases of $a = 1$ for equal proton and electron luminosities and $a = 100$ for a proton-dominated jet.

3. Hadronic processes at the base of the jet

In the one-zone approximation (Khangulyan et al. 2007), we assume that shock acceleration of the particles takes place in the jet at distances from z_0 to $z_{max} = 5z_0$ from the compact object. The injection rate is assumed to be a power law in the particle energy $N'(E') = K_0 E'^{-2}$ (GeV^{-1} cm^{-3}). The corresponding current can be written as $J'(E') = cN'(E')$ in the reference frame co-moving with the jet particles. The conservation of the number of particles is satisfied if the current evolves with z as (see Ghisellini et al. 1985)

$$J'(E', z) = K_0 c \left(\frac{z_0}{z}\right)^2 E'^{-2} \left(\mathrm{GeV^{-1} s^{-1} cm^{-2}}\right). \quad (3)$$

The continuity equation in the case of no time dependence and in the absence of sinks, implies that the injection or source function of particles must satisfy

$$Q'(E', z) = \nabla \cdot J'(E', z)\,\hat{z},$$

so that we have

$$Q(E', z) = Q_0 \left(\frac{z_0}{z}\right)^3 E'^{-2} \left(\mathrm{GeV^{-1} cm^{-3} s^{-1}}\right). \quad (4)$$

In the observer reference frame, whose line of sight makes an angle θ with the jet, since $E' = \Gamma_b(E - \beta_b \cos\theta \sqrt{E^2 - m^2c^4})$, $\mathrm{d}V'/\mathrm{d}V = \Gamma_b$, and

$$\frac{\mathrm{d}E'}{\mathrm{d}E} = \Gamma_b - \frac{\beta_b E \cos\theta}{\sqrt{E^2 - m^2c^4}}, \quad (5)$$

it follows that

$$Q(E, z) = Q_0 \left(\frac{z_0}{z}\right)^3 \Gamma_b^{-1} \left(E - \beta_b \sqrt{E^2 - m^2c^4} \cos\theta\right)^{-2} \times \left|\Gamma_b - \frac{\beta_b E \cos\theta}{\sqrt{E^2 - m^2c^4}}\right|, \quad (6)$$

Table 1. Parameters of the model.

Parameter	Value
L_k: jet power	10^{38} erg s^{-1}
q_{rel}: jet's content of relativistic particles	0.1
a: hadron-to-lepton ratio	1, 100
z_0: jet's launching point	10^8 cm
z_{max}: extent of acceleration region	5 z_0
Γ_b: jet's bulk Lorentz factor	1.25
ξ: jet's half-opening angle	1.5, 5°
θ: viewing angle	30°
η: acceleration efficiency	0.1

where Γ_b is the bulk Lorentz factor of the jet. The normalization constant Q_0 is obtained by specifying the power in relativistic particles:

$$L_{e,p} = \int_V \mathrm{d}^3 r \int_{E_{e,p}^{(min)}}^{E_{e,p}^{(max)}} \mathrm{d}E_{e,p} E_{e,p} Q_{e,p}(E_{e,p}, z). \quad (7)$$

The minimum energies are $E_e^{(min)} = 1$ MeV and $E_p^{(min)} = 1.2$ GeV, and the maximum energies will be obtained in the next section by equating the acceleration rate to the energy loss rate. The parameters of our model are summarized in Table 1.

3.1. Accelerating and cooling rates: maximum energies

The rate of acceleration of the particles to an energy E, $t_{acc}^{-1} = E^{-1}\mathrm{d}E/\mathrm{d}t$, is given by

$$t_{acc}^{-1} \approx \eta \frac{c\,e\,B}{E_p}, \quad (8)$$

where we consider $\eta = 0.1$ for the acceleration efficiency. This corresponds to the case of an efficient accelerator, as expected at the base of the jet where shocks are mildly relativistic; see, e.g. Begelman et al. (1990).

Charged particles of mass m and energy $E = \gamma mc^2$ will emit synchrotron radiation at a rate

$$t_{sync}^{-1} = \frac{4}{3}\left(\frac{m_e}{m}\right)^3 \frac{\sigma_T B^2}{m_e c\, 8\pi}\gamma. \quad (9)$$

In the jet at a distance z from the compact object, the density of cold particles is

$$n(z) = \frac{(1 - q_{rel})}{\Gamma_b m_p c \pi r_j^2 v_b} L_k. \quad (10)$$

The rate of pp collisions of the relativistic protons with the cold ones is then given by

$$t_{pp}^{-1} = n(z)\, c\, \sigma_{pp}^{(inel)}(E_p) K_{pp}, \quad (11)$$

where the inelasticity coefficient is $K_{pp} \approx 1/2$ and the corresponding cross section for inelastic pp interactions can be approximated by (Kelner et al. 2006)

$$\sigma_{pp}^{(inel)}(E_p) = \left(34.3 + 1.88L + 0.25L^2\right) \times \left[1 - \left(\frac{E_{th}}{E_p}\right)^4\right]^2 \times 10^{-27}\ \mathrm{cm}^2, \quad (12)$$

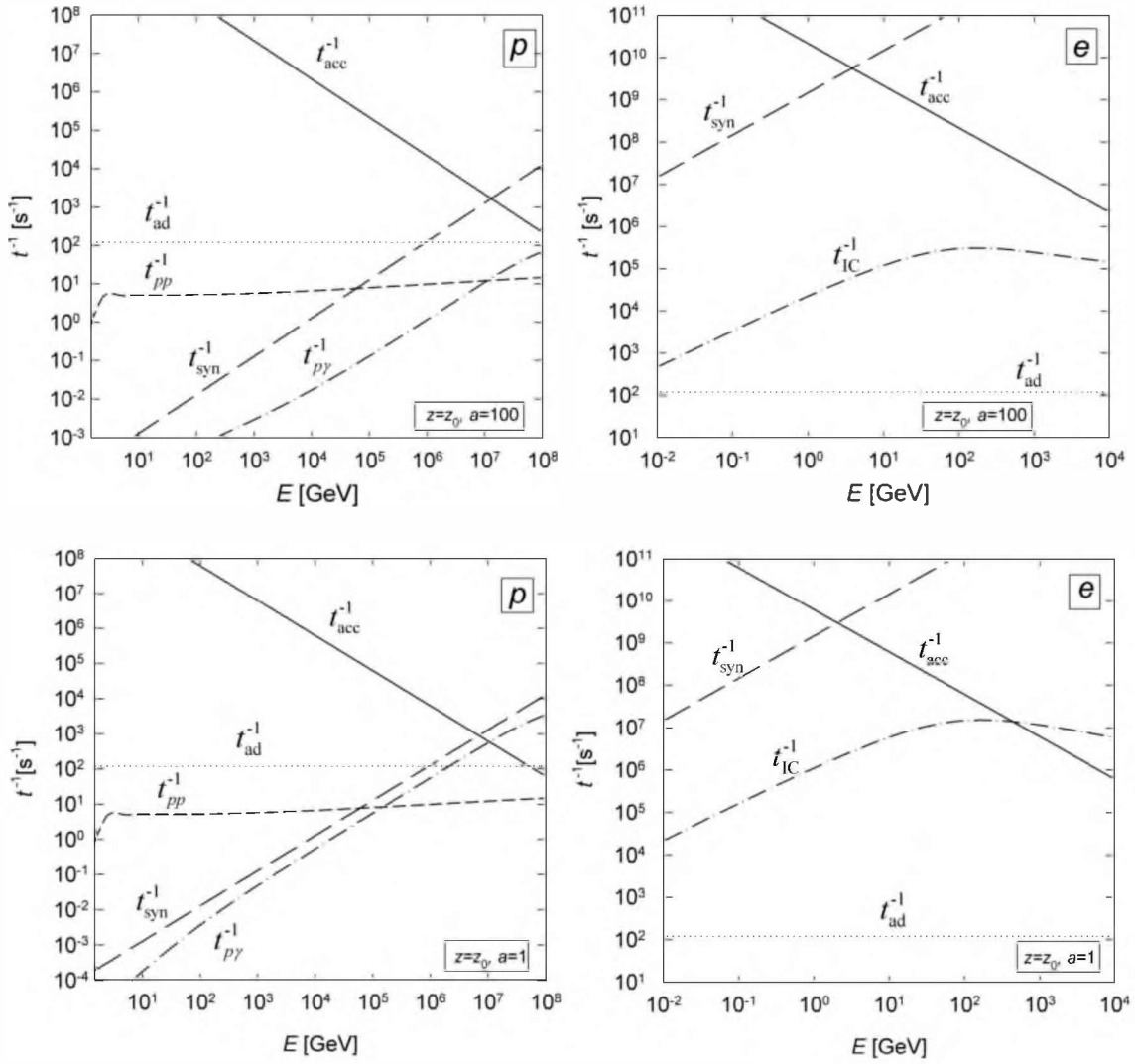

Fig. 2. Accelerating and cooling rates for protons (*left panels*) and for electrons (*right panels*) at the base of the jets. The *top panels* correspond to $a = 100$ and the *bottom ones* to $a = 1$. Plots shown: (solid lines), adiabatic cooling rates (dotted lines), synchrotron cooling rates (long-dashed lines), pp cooling rates (short-dashed lines), $p\gamma$ cooling rates (dash-dotted lines, *left panels*), and IC cooling rates (dash-dotted lines, *right panels*).

where $L = \ln(E_p/1000\ \mathrm{GeV})$ and $E_{th} = 1.2$ GeV. Because the jet is expanding with a lateral velocity ($v_b \tan\xi$) the adiabatic cooling rate is (Bosch-Ramon et al. 2006)

$$t^{-1}_{ad} = \frac{2}{3}\frac{v_b}{z}. \tag{13}$$

We estimate the maximum energies achieved by the particles by equating $t^{-1}_{acc}(E^{(max)}) = t^{-1}_{loss}(E^{(max)})$. In the case of electrons, we assume $t^{-1}_{loss} = t^{-1}_{syn} + t^{-1}_{ad}$, and for protons $t^{-1}_{loss} = t^{-1}_{syn} + t^{-1}_{ad} + t^{-1}_{pp}$. At the base of the jet, for $a = 100$, we obtain

$$E^{(max)}_e(z_0) \approx 7\ \mathrm{GeV} \tag{14}$$

and

$$E^{(max)}_p(z_0) \approx 10^7\ \mathrm{GeV}. \tag{15}$$

We show in Fig. 2 the above rates for electrons and protons, as well as the cooling rates due to $p\gamma$ and IC interactions that arise due to the photons from the synchrotron emission (see next section).

3.2. Proton and electron distributions

In the one-zone approximation the particle distribution independent of time, i.e., in a steady state, can be obtained as the solution of the following transport equation:

$$\frac{\partial N(E,z)b(E,z)}{\partial E} + t^{-1}_{esc}(z)\, N(E,z) = Q(E,z), \tag{16}$$

where $b(E,z) = -E\, t^{-1}_{loss}(E,z)$ and

$$t^{-1}_{esc}(z) \approx \frac{c}{z_{max} - z} \tag{17}$$

is the escape rate.

The corresponding solution is

$$N(E,z) = \frac{1}{|b(E)|}\int_E^{E^{(max)}} dE'\, Q(E',z) \times \exp\left\{-t^{-1}_{esc}(z)\,\tau(E,E')\right\}, \tag{18}$$

with

$$\tau(E,E') = \int_E^{E'} \frac{dE''}{|b(E'')|}.$$

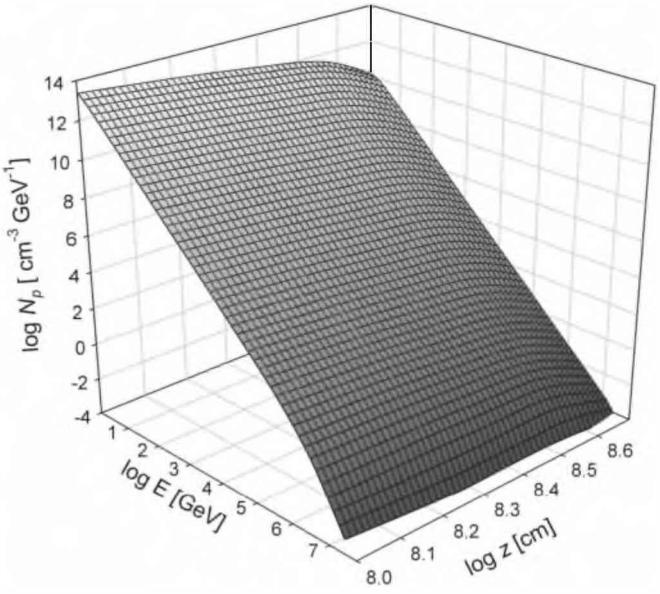

Fig. 3. Proton distribution as a function of energy and distance to the compact object.

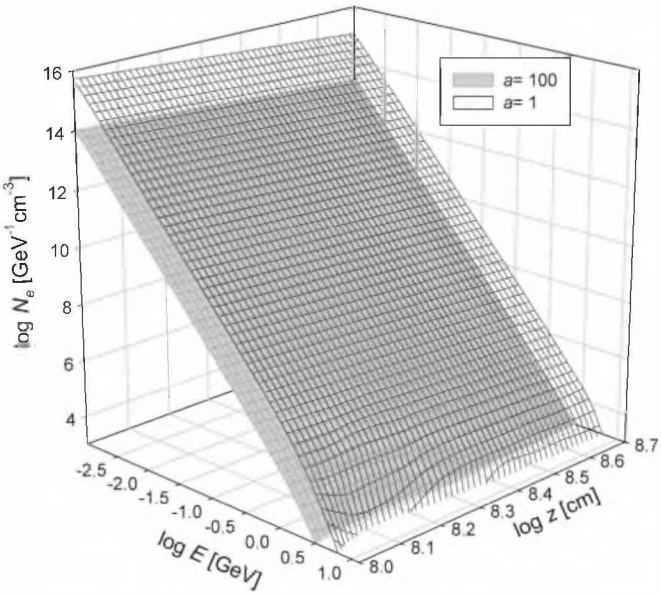

Fig. 4. Electron distribution as a function of energy and distance to the compact object. The cases of $a = 1$ and $a = 100$ are shown in gray and transparent surfaces, respectively.

We notice that here the effect of particle acceleration is included through the injection function which depends on the energy with a power law in the frame co-moving with the bulk of the jet.

We show the obtained distributions as a function of energy and z in Figs. 3 and 4 for protons and electrons, respectively. It can be seen from the latter figure that if $a = 1$ the number of electrons is higher than for $a = 100$, as expected. For protons, we show the case of $a = 100$, but it does not differ significantly if $a = 1$.

3.3. Synchrotron radiation

Both the protons and electrons will emit synchrotron radiation. The power radiated by a single particle of energy E and pitch angle α is (e.g. Blumenthal & Gould 1970)

$$P_{\rm syn}(E_\gamma, E, z, \alpha) = \frac{\sqrt{3}e^3 B(z)}{4\pi mc^2 h}\frac{E_\gamma}{E_{\rm cr}}\int_{E_\gamma/E_{\rm cr}}^{\infty} {\rm d}\zeta K_{5/3}(\zeta), \quad (19)$$

where $K_{5/3}(\zeta)$ is the modified Bessel function of order 5/3 and

$$E_{\rm cr} = \frac{3heB(z)\sin\alpha}{4\pi mc}\left(\frac{E}{mc^2}\right)^2.$$

The power per unit energy of the synchrotron photons is

$$\varepsilon_{\rm syn}^{\rm (e,p)}(E_\gamma) = \int {\rm d}\Omega_\alpha \int_{E_{\rm e,p}^{\rm (min)}}^{E_{\rm e,p}^{\rm (max)}} {\rm d}E\, P_{\rm syn} N_{\rm e,p}(E, z), \quad (20)$$

and the total luminosity can be obtained by integrating in the volume of the region of acceleration

$$L_{\rm syn}^{\rm (e,p)}(E_\gamma) = \int_V {\rm d}^3 r\, E_\gamma \varepsilon_{\rm syn}^{\rm (e,p)}. \quad (21)$$

The results for synchrotron radiation of protons and electrons are shown in Fig. 5 with $a = 1$ in the right panel and $a = 100$ in the left panel.

3.4. Inverse Compton and $p\gamma$ interactions

The synchrotron photons will, in turn, serve as targets for electrons and protons themselves. Locally, the corresponding radiation density can be expressed as

$$N_{\rm ph}(\epsilon, z) \approx \frac{\varepsilon_{\rm syn}}{\epsilon}\frac{r_{\rm j}(z)}{c}\left({\rm GeV}^{-1}{\rm cm}^{-3}\right). \quad (22)$$

Electrons will interact by Inverse-Compton scatterings at a rate

$$t_{\rm IC}^{-1}(E, z) = \frac{4}{3}\frac{\sigma_{\rm T}\rho_{\rm ph}}{m_{\rm e}c}\gamma_{\rm e}, \quad (23)$$

where

$$\rho_{\rm ph} = \int \epsilon\, N_{\rm ph}(\epsilon){\rm d}\epsilon$$

is the corresponding energy density in photons. As protons interact with synchrotron photons, they lose energy due to photopion production at a rate

$$t_{p\gamma}^{-1}(E, z) = \frac{c}{2\gamma_{\rm p}^2}\int_{\frac{\epsilon_{\rm th}}{2\gamma_{\rm p}}}^{\infty} {\rm d}\epsilon \frac{N_{\rm ph}(\epsilon, z)}{\epsilon^2} \times \int_{\epsilon_{\rm th}}^{2\epsilon\gamma_{\rm p}} {\rm d}\epsilon' \sigma_{p\gamma}^{(\pi)}(\epsilon') K_{p\gamma}^{(\pi)}(\epsilon')\,\epsilon'. \quad (24)$$

Here, $\epsilon_{\rm th} = 150$ MeV and we adopt the cross section (Atoyan & Dermer 2003, see also Kelner & Aharonian 2008)

$$\sigma_{p\gamma}^{(\pi)} = \Theta(\epsilon' - 200\ {\rm MeV})\,\Theta(500\ {\rm MeV} - \epsilon')\,3.4\times10^{-28}\ {\rm cm}^2 + \Theta(\epsilon' - 500\ {\rm MeV})\,1.2\times10^{-28}\ {\rm cm}^2, \quad (25)$$

and the inelasticity as

$$K_{p\gamma}^{(\pi)} = \Theta(\epsilon' - 200\ \ {\rm MeV})\,\Theta(500\ \ {\rm MeV} - \epsilon')\,0.2 + \Theta(\epsilon' - 500\ \ {\rm MeV})\,0.6. \quad (26)$$

The obtained IC and $p\gamma$ cooling rates are shown in Fig. 2. It can be seen from this plot that the dominant mechanisms for energy loss are those discussed at the beginning of this section.

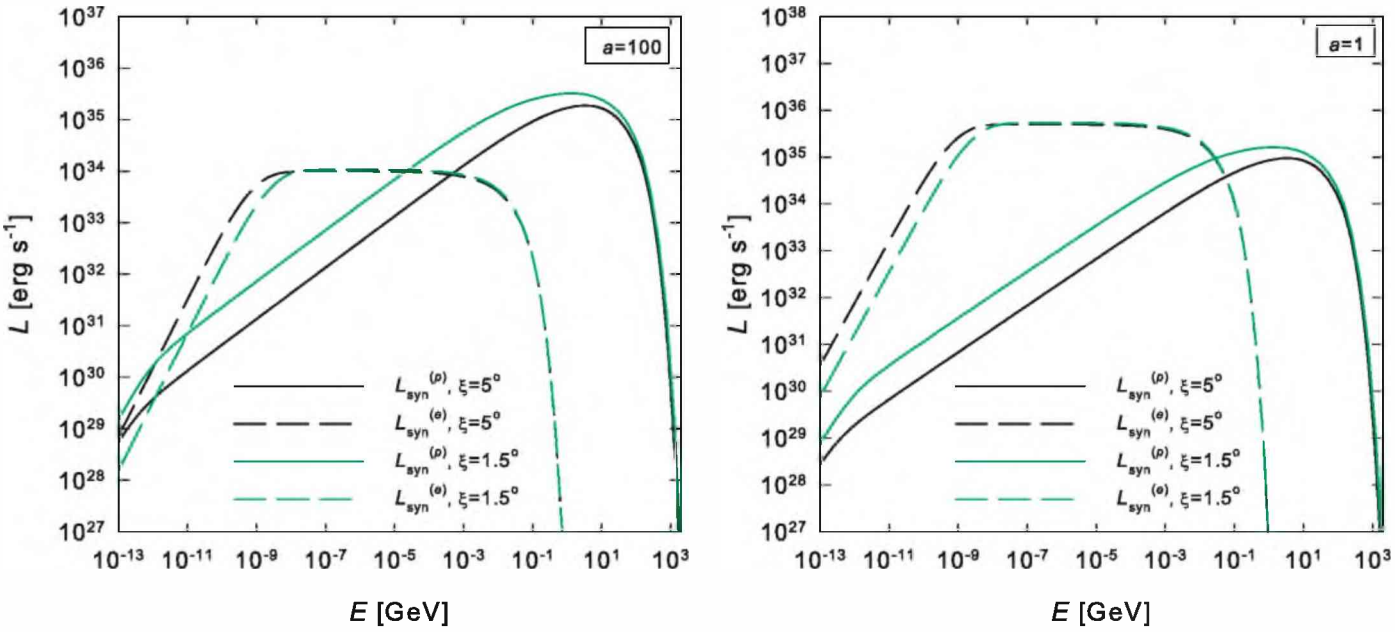

Fig. 5. Synchrotron luminosity emitted by protons (solid lines) and by electrons (dashed lines). Black lines correspond to $\xi = 5°$ and green lines to $\xi = 1.5°$. The cases of $a = 1$ and $a = 100$ are shown in *the right and left panels*, respectively.

4. Magnetic effects on secondary particles

The primary relativistic protons will produce pions through inelastic interactions with matter and radiation. Pions will decay to muons and neutrinos, and muons will also decay, giving neutrinos and electrons:

$$\pi^- \rightarrow \mu^- \bar{\nu}_\mu \rightarrow e^- \nu_\mu \bar{\nu}_e \bar{\nu}_\mu \quad (27)$$

$$\pi^+ \rightarrow \mu^+ \nu_\mu \rightarrow e^+ \bar{\nu}_\mu \nu_e \nu_\mu. \quad (28)$$

But before decaying, pions and muons may interact, losing energy according to the processes discussed in the previous section. In the case of pions,

$$b_\pi(E,z) = \frac{dE}{dt} = -E(t_{syn}^{-1} + t_{ad}^{-1} + t_{\pi p}^{-1} + t_{\pi\gamma}^{-1}). \quad (29)$$

For the πp interactions we consider

$$t_{\pi p}^{-1}(E,z) \approx \frac{n(z)\, c\, \sigma_{\pi p}^{(inel)}(E)}{2}, \quad (30)$$

with $\sigma_{\pi p}(E) \approx \frac{2}{3}\sigma_{pp}^{inel}(E)$ based on the proton being formed by three valence quarks, while the pion is formed by two (Gaisser 1990). As for the $\pi\gamma$ interactions, we estimate a cooling rate using expression (24) with the replacement $\sigma_{p\gamma}^{(\pi)} \rightarrow (2/3)\sigma_{p\gamma}^{(\pi)}$. For muons, we have

$$b_\mu(E,z) = -E\left(t_{syn}^{-1} + t_{ad}^{-1} + t_{IC}^{-1}\right). \quad (31)$$

In Fig. 6 we show the different rates corresponding to $z = z_0$ for pions in the left panels and for muons in the right panels. The cases with $a = 100$ are shown in the upper panels and the cases with $a = 1$ in the lower panels. We have included the rate of decay and escape as

$$t_{\pi,\mu}^{-1}(E,z) = t_{esc}^{-1}(z) + t_{dec}^{-1}(E), \quad (32)$$

where $t_{dec}^{-1} = [2.6 \times 10^{-8}\gamma_\pi]^{-1}(s^{-1})$ for pions and $t_{dec}^{-1} = [2.2 \times 10^{-6}\gamma_\mu]^{-1}(s^{-1})$ for muons.

4.1. Pion injection

The injection function of pions produced by pp interactions is given by

$$Q_\pi^{(pp)}(E,z) = n(z)\, c \int_{\frac{E}{E_p^{(max)}}}^1 \frac{dx}{x} N_p\left(\frac{E}{x}, z\right) \times F_\pi^{(pp)}\left(x, \frac{E}{x}\right) \sigma_{pp}^{(inel)}\left(\frac{E}{x}\right) \quad (33)$$

where

$$F_\pi^{(pp)}\left(x, \frac{E}{x}\right) = 4\alpha B_\pi x^{\alpha-1}\left(\frac{1-x^\alpha}{1+rx^\alpha(1-x^\alpha)}\right)^4 \times \left(\frac{1}{1-x^\alpha} + \frac{r(1-2x^\alpha)}{1+rx^\alpha(1-x^\alpha)}\right)\left(1 - \frac{m_\pi c^2}{xE_p}\right)^{1/2} \quad (34)$$

is the distribution of pions produced per pp collision, with $x = E/E_p$, $B_\pi = a' + 0.25$, $a' = 3.67 + 0.83L + 0.075L^2$, $r = 2.6/\sqrt{a'}$, and $\alpha = 0.98/\sqrt{a'}$ (see Kelner et al. 2006).

The injection function for charged pions from $p\gamma$ interactions is

$$Q_\pi^{(p\gamma)}(E,z) = \int_E^{E_p^{(max)}} dE_p N_p(E_p,z)\, \omega_{p\gamma}(E_p,z) \times \mathcal{N}_\pi(E_p)\, \delta(E - 0.2E_p) = 5\, N_p(5E,z)\, \omega_{p\gamma}(5E,z)\, \mathcal{N}_\pi(5E). \quad (35)$$

Here the $p\gamma$ collision frequency is

$$\omega_{p\gamma}(E_p,z) = \frac{c}{2\gamma_p^2}\int_{\frac{\epsilon_{th}}{2\gamma_p}}^\infty d\epsilon \frac{N_{ph}(\epsilon,z)}{\epsilon^3}\int_{\epsilon_{th}}^{2\epsilon\gamma_p} d\epsilon' \sigma_{p\gamma}^{(\pi)}(\epsilon')\,\epsilon', \quad (36)$$

and the mean number of positive and negative pions is

$$\mathcal{N}_\pi \approx \frac{p_1}{2} + 2p_2, \quad (37)$$

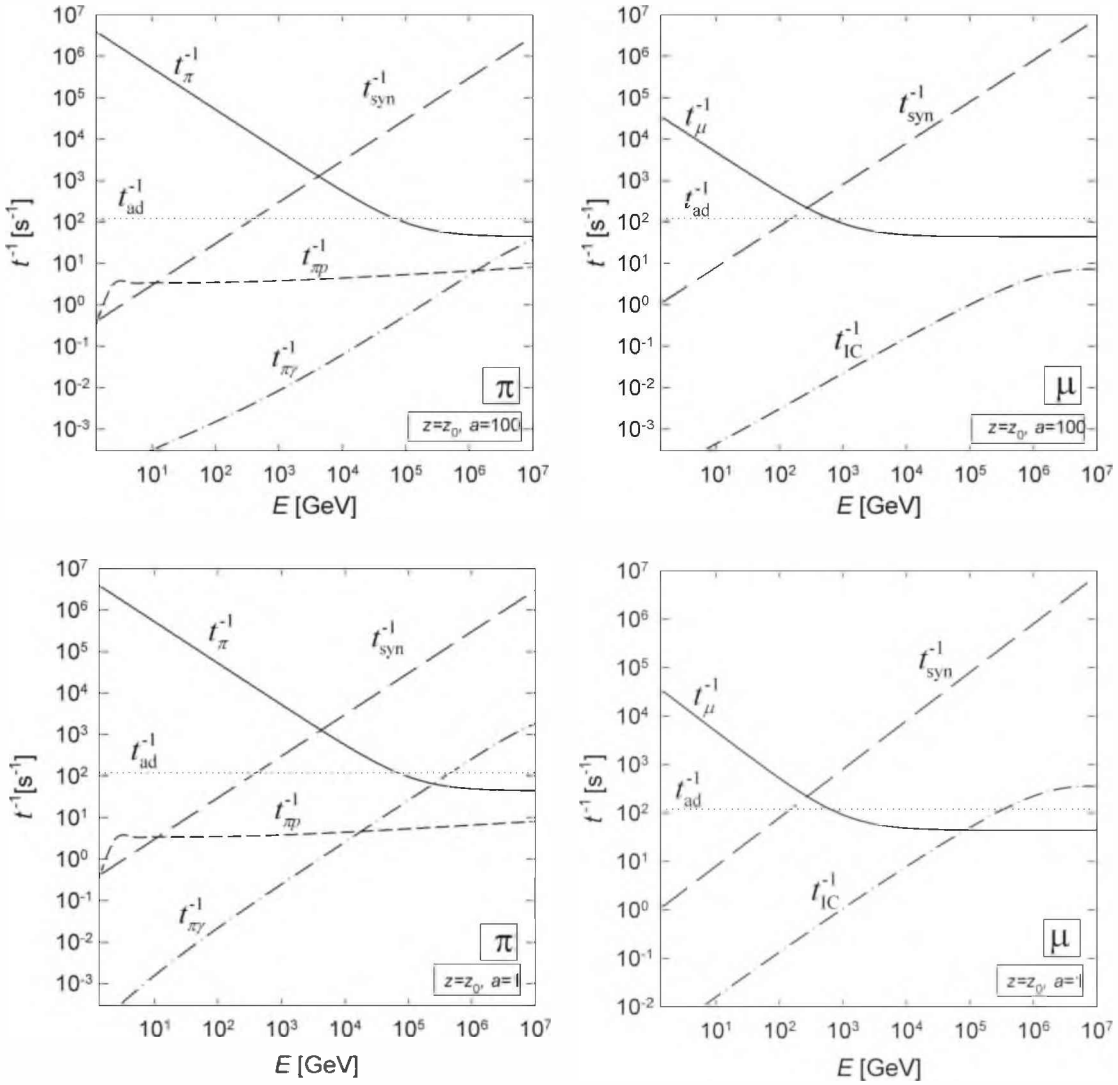

Fig. 6. Cooling rates for pions (*left panels*) and for muons (*right panels*) at the base of the jets. The *top panels* correspond to $a = 100$ and the *bottom ones* to $a = 1$. Plots shown: adiabatic cooling rates (dotted lines), synchrotron cooling rates (long-dashed lines), πp cooling rates (short-dashed lines), $\pi\gamma$ cooling rates (dash-dotted lines, left panels), and IC cooling rates (dash-dotted lines, right panels). The decay plus escape rates are also shown (solid lines).

with p_1 and $p_2 = 1 - p_1$ as the probabilities of single pion and multi-pion production, respectively. These are related to the mean inelasticity function $\bar{K}_{p\gamma} = t_{p\gamma}^{-1}\omega_{p\gamma}^{-1}$ by

$$p_1 = \frac{K_2 - \bar{K}_{p\gamma}}{K_2 - K_1}, \tag{38}$$

where $K_1 = 0.2$ and $K_2 = 0.6$.

4.2. Steady-state distribution of charged pions

The steady pion distribution obeys the transport Eq. (16) with the replacement $t_{\rm esc}^{-1} \to t_{\pi}^{-1}(E, z)$. The solution is

$$N_\pi(E,z) = \frac{1}{|b_\pi(E)|}\int_E^{E^{(\max)}} {\rm d}E' Q(E',z) \times \exp\{-\tau_\pi(E,E')\}. \tag{39}$$

with

$$\tau_\pi(E', E) = \int_{E'}^{E} \frac{{\rm d}E'' t_\pi^{-1}(E,z)}{|b_\pi(E'')|}. \tag{40}$$

Depending on whether we use $Q_\pi^{(pp)}(E,z)$ or $Q_\pi^{(p\gamma)}(E,z)$ in this last expression, we obtain $N_\pi^{(pp)}(E,z)$ or $N_\pi^{(p\gamma)}(E,z)$.

4.3. Muon steady state distribution

As discussed in Lipari et al. (2007), to take the muon energy loss into account, it is necessary to consider the production of left handed and right handed muons separately, which have different decay spectra:

$$\frac{{\rm d}n_{\pi^-\to\mu_L^-}}{{\rm d}E_\mu}(E_\mu; E_\pi) = \frac{r_\pi(1-x)}{E_\pi x(1-r_\pi)^2}\Theta(x - r_\pi) \tag{41}$$

$$\frac{{\rm d}n_{\pi^-\to\mu_R^-}}{{\rm d}E_\mu}(E_\mu; E_\pi) = \frac{(x - r_\pi)}{E_\pi x(1-r_\pi)^2}\Theta(x - r_\pi), \tag{42}$$

with $x = E_\mu/E_\pi$ and $r_\pi = (m_\mu/m_\pi)^2$.

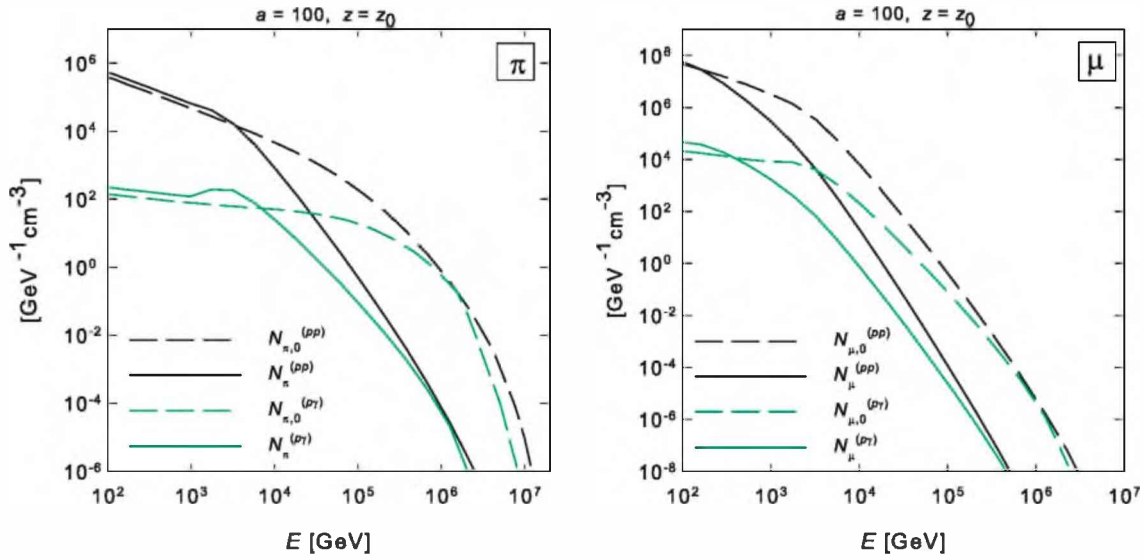

Fig. 7. Pion and muon distributions at the base of the jet in *the left and right panels* respectively, originated by pp interactions (black lines) and by $p\gamma$ interactions (green lines). Solid lines: distributions obtained considering cooling. Dashed lines: distributions obtained neglecting cooling.

The injection function of negative left handed and positive right handed muons is

$$Q_{\mu_L^-\mu_R^+}(E_\mu,z) = \int_{E_\mu}^{E^{(\max)}} \mathrm{d}E_\pi t^{-1}_{\pi,\mathrm{dec}}(E_\pi) \times \left(N_{\pi^-}(E_\pi,z)\frac{\mathrm{d}n_{\pi^-\to\mu_L^-}}{\mathrm{d}E_\mu}(E_\mu;E_\pi) + N_{\pi^+}(E_\pi,z)\frac{\mathrm{d}n_{\pi^-\to\mu_R^-}}{\mathrm{d}E_\mu}(E_\mu;E_\pi)\right). \quad (43)$$

Because CP invariance implies that $\mathrm{d}n_{\pi^-\to\mu_L^-}/\mathrm{d}E_\mu = \mathrm{d}n_{\pi^+\to\mu_R^+}/\mathrm{d}E_\mu$, and since the above distribution obtained for all charged pions is $N_\pi(E_\pi,z) = N_{\pi^+}(E_\pi,z) + N_{\pi^-}(E_\pi,z)$, it follows that

$$Q_{\mu_L^-\mu_R^+}(E_\mu,z) = \int_{E_\mu}^{E^{(\max)}} \mathrm{d}E_\pi t^{-1}_{\pi,\mathrm{dec}}(E_\pi) \times N_\pi(E_\pi,z)\frac{\mathrm{d}n_{\pi^-\to\mu_L^-}}{\mathrm{d}E_\mu}(E_\mu;E_\pi). \quad (44)$$

Similarly,

$$Q_{\mu_R^-\mu_L^+}(E_\mu,z) = \int_{E_\mu}^{E^{(\max)}} \mathrm{d}E_\pi t^{-1}_{\pi,\mathrm{dec}}(E_\pi) \times N_\pi(E_\pi,z)\frac{\mathrm{d}n_{\pi^-\to\mu_R^-}}{\mathrm{d}E_\mu}(E_\mu;E_\pi). \quad (45)$$

For illustration, we show the obtained pion and muon distributions at $z = z_0$ in Fig. 7, for the cases of production caused by pp and $p\gamma$ interactions. In these plots, we also show the particle distributions that correspond to no energy losses. The solution corresponding to no energy losses will simply have the form

$$N_{\pi,0}(E,z) = \frac{Q_\pi(E,z)}{t_\pi^{-1}(E,z)}, \quad (46)$$

$$N_{\mu,0}(E,z) = \frac{Q_\mu(E,z)}{t_\mu^{-1}(E,z)}. \quad (47)$$

We also note that the muon distributions shown include the contributions of the muons with different helicity states added up.

4.4. Neutrino emission

The total emissivity of neutrinos,

$$Q_\nu(E,z) = Q_{\pi\to\nu}(E,z) + Q_{\mu\to\nu}(E,z),$$

is the sum of the contribution of direct pion decays plus that of muon decays:

$$Q_{\pi\to\nu}(E,z) = \int_E^{E_{\max}} \mathrm{d}E_\pi t^{-1}_{\pi,\mathrm{dec}}(E_\pi)N_\pi(E_\pi,z) \times \frac{\Theta(1-r_\pi-x)}{E_\pi(1-r_\pi)}, \quad (48)$$

with $x = E/E_\pi$, and

$$Q_{\mu\to\nu}(E,z) = \sum_{i=1}^{4}\int_E^{E_{\max}} \frac{dE_\mu}{E_\mu} t^{-1}_{\mu,\mathrm{dec}}(E_\mu)N_{\mu_i}(E_\mu,z) \times \left[\frac{5}{3} - 3x^2 + \frac{4}{3}x^3 + \left(3x^2 - \frac{1}{3} - \frac{8x^3}{3}\right)h_i\right]. \quad (49)$$

In this last expression, $x = E/E_\mu$, $\mu_{\{1,2\}} = \mu_L^{\{-,+\}}$, $\mu_{\{3,4\}} = \mu_R^{\{-,+\}}$, and

$$h_{\{1,2\}} = -h_{\{3,4\}} = -1, \quad (50)$$

according to Lipari et al. (2007).

The neutrino intensity (in units of $\mathrm{GeV}^{-1}\mathrm{s}^{-1}$),

$$I_\nu(E) = \int_V \mathrm{d}^3 r\; Q_\nu(E,z), \quad (51)$$

is shown in Fig. 8 for the different values of a and the jet half-opening angle ξ.

The differential flux of neutrinos arriving at the Earth can be obtained as

$$\frac{\mathrm{d}\Phi_\nu}{\mathrm{d}E} = \frac{1}{4\pi \mathrm{d}^2} I_\nu(E). \quad (52)$$

This quantity, weighted by the squared energy, is shown in Fig. 9 for a source at a distance $d = 2$ kpc, different values of the jet opening angle, and different values of a. As a guide, we also include a typical upper limit as derived from AMANDA-II data, as well as the expected sensitivity for the next generation neutrino telescope (Halzen 2006, see also Aiello et al. 2007).

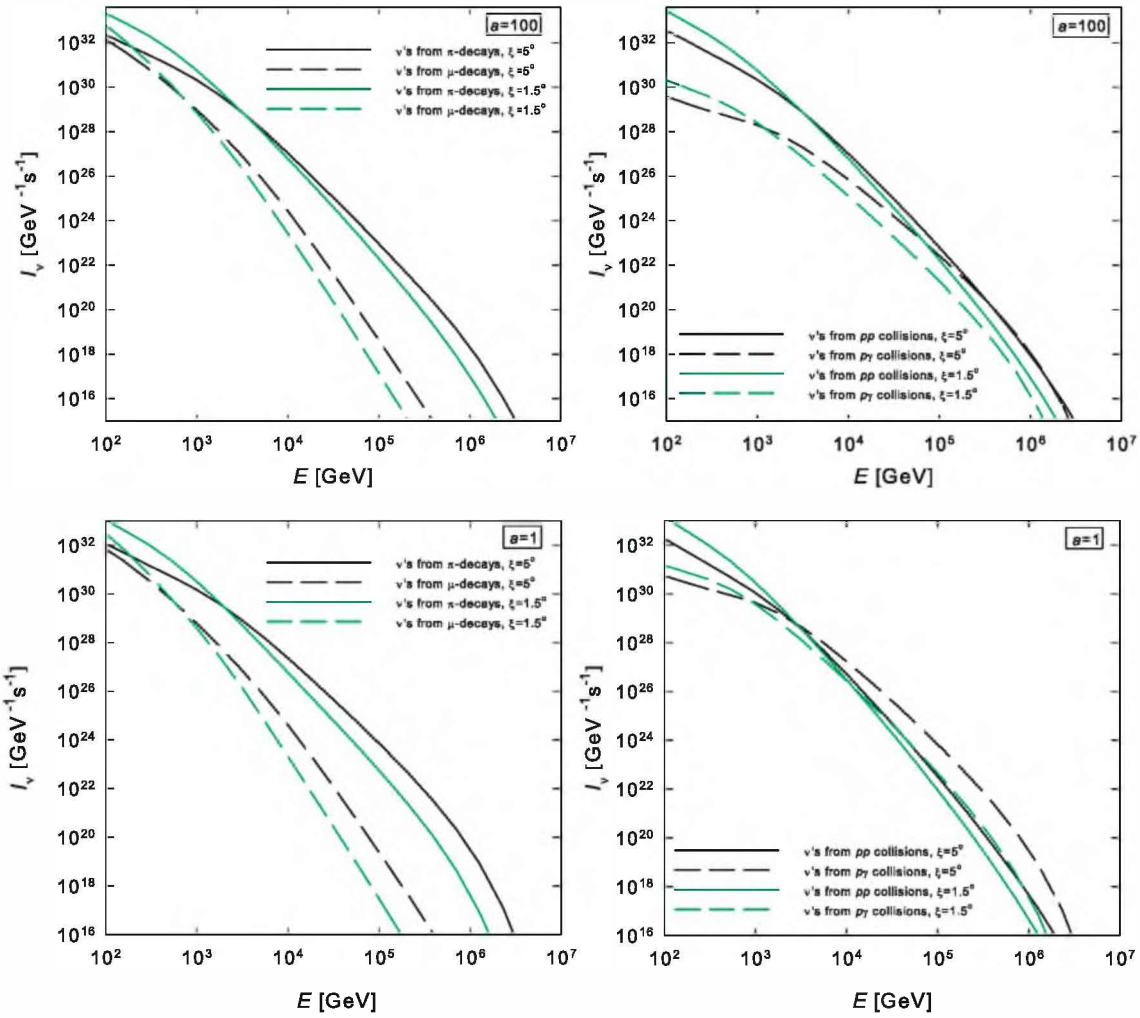

Fig. 8. Different contributions of the neutrino intensity produced at the base of the jet. The cases of $a = 100$ and $a = 1$ are shown in the *top and bottom panels*, respectively. Black lines correspond to $\xi = 5°$ and green lines to $\xi = 1.5°$. *Left panels*: contributions from direct pion decays (solid lines) and from muon decays (dashed lines). *Right panels*: contributions due to pp interactions (solid lines) and due to $p\gamma$ interactions (dashed lines).

5. Neutrino production through jet-wind interactions

In high-mass microquasars, the donor star can present a strong wind with dense *clumps* of matter (Romero et al. 2007). In this section, we apply a very simplistic model to estimate the possible high-energy neutrino emission produced by the interaction of such clumps with jet matter.

We consider that the matter composing the clump that is successfully interacting with the jet is uniformly distributed within a slice of the jet with a thickness equal to the radius of the clump. This enables us to apply the same method we used in the previous sections, where the one-zone acceleration region was placed in the vicinity of the compact object. In this case, the acceleration zone will be located at high distances from the compact object, say around half the distance to the companion star. There, the density of jet matter is two or three orders of magnitude less than that of the clumps, and the magnetic field is expected to be much weaker than close to the compact star.

We assume that the clump density is $\rho_c = 10^{-12}$ g cm^{-3}, and we consider two different radii: $R_c = 10^{11}$ cm and $R_c = 10^{10}$ cm. The relativistic particles are accelerated in a region of length R_c. We assume a lower acceleration efficiency, $\eta = 0.01$, and we can calculate, as above, the different cooling rates. In doing this, we consider that the density of cold matter in the acceleration zone is

$$n_c(z) = \frac{4}{3}\frac{R_c^2 \rho_c}{r_j^2 m_p}. \tag{53}$$

For illustration we show in Fig. 10 the obtained acceleration and cooling rates, in the case of a successful jet-clump interaction at $z = 10^{12}$ cm.

We consider that clumps can penetrate the jet at distances $\gtrsim 5 \times 10^{11}$ cm, where the density of cold protons in the jet begins to decrease below 10^9 cm^{-3}. The protons and electrons are then injected in a slice of thickness R_c using expression (6), and normalizing it through Eq. (7) using $q_{rel} = 0.1$ and $a = 100$. The steady state distributions of protons and electrons are found using expression (18) taking $T_{esc} = R_c/v_b$. Next, the injection of pions is found to be dominated by the contribution of pp interactions, given by expression (33).

According to Fig. 10, the decay process of the pions and muons dominate in almost all the relevant energy range, so in

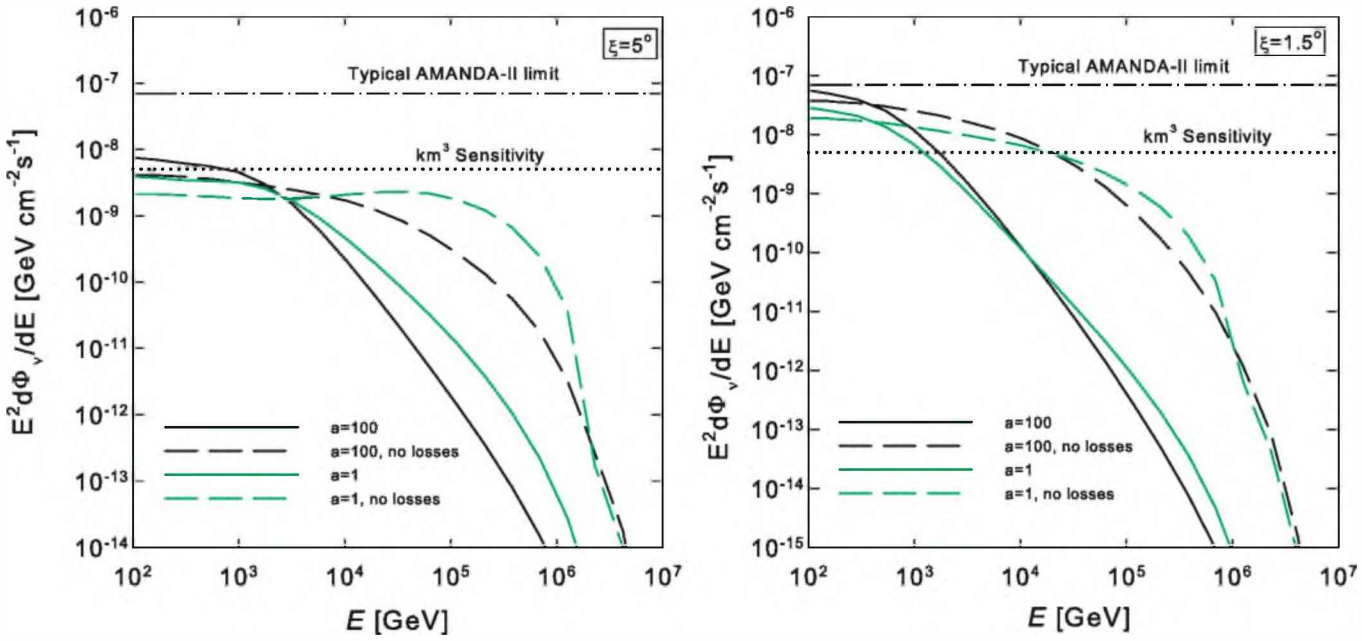

Fig. 9. Differential neutrino fluxes weighted by the squared energy. The cases of $\xi = 5°$ and $\xi = 1.5°$ are shown in *the left and right panels*. respectively. Black lines correspond to $a = 100$ and green lines to $a = 1$. Solid (dashed) lines: losses of secondary pions and muons considered (neglected).

a first approximation we can neglect losses so that

$$N_\pi(E,z) \approx \frac{Q_\pi^{(pp)}(E,z)}{t_\pi^{-1}(E,z)}. \tag{54}$$

Substituting this pion distribution in expressions (44) and (45), we can obtain

$$N_\mu(E,z) \approx \frac{Q_\mu^{(pp)}(E,z)}{t_\mu^{-1}(E,z)}. \tag{55}$$

Following the steps discussed in Sect. 4.4, the neutrino intensity and differential flux can be obtained. The corresponding differential flux of neutrinos weighted by the squared energy is shown in Fig. 11. There we show the results corresponding to the half-opening angles $\xi = 1.5°$ and $\xi = 5°$ for $R_c = 10^{10}$ cm and $R_c = 10^{11}$ cm. A duty cycle of 10% was adopted, meaning that the clumps interact with the jet successfully, on average 10% of the time. The neutrinos produced are to be observed with cubic kilometer detectors over a long period of time (several years).

6. Discussion

The presence of an equipartition magnetic field in the jets of microquasars implies a strong attenuation in the high energy spectra of pions and muons that could be produced by hadronic interactions. This effect is found to be relevant in the vicinity of the compact object, as can be seen in Fig. 7. The neutrino flux expected in this case is significantly reduced at energies above 1 TeV, which is the range to be probed by upcoming neutrino telescopes such as IceCube (see Fig. 9).

Due to the lifetime of pions being shorter than that of muons, neutrinos produced by the direct decay of pions dominate over those originated by muon decays, since muons lose a significant fraction of their energy by synchrotron radiation before decaying (see Fig. 8, left panels).

With $a = 1$, i.e. for equal power carried in relativistic protons and electrons, the neutrino contribution due to pp interactions is dominant at low energies, $E \lesssim 10$ TeV for $\xi = 1.5°$ and $E \lesssim 3$ TeV for $\xi = 5°$. At higher energies, the $p\gamma$ contribution becomes important (see Fig. 8, bottom right panel). However, in a case with $a = 100$, which seems more realistic (Heinz 2006), pp interactions provide the most relevant mechanism for neutrino production.

For windy microquasars, an additional neutrino contribution can arise from jet-wind interactions. In this case, the clumps composing the stellar wind could interact with the jet at large distances from the compact object ($z \gtrsim 5 \times 10^{11}$ cm), where the jet particle density is much lower than that of the clumps. The magnetic field in those regions of the jet is expected to be much lower than at the jet base. This leads to a negligible synchrotron energy loss of secondary pions and muons, and probably to the production of a neutrino flux whose detectability depends on several factors such as the density and size of the clumps, and the duty cycle corresponding to this type of interactions.

The jet half-opening angle is another parameter that matters. We considered two cases: $\xi = 5°$ and $\xi = 1.5°$. The first value is often assumed in the literature and the second one is another possibility of a more collimated outflow (notice that for SS433, $\xi \approx 0.6°$). For wide opening angles, the magnetic energy density is lower than for narrow ones, and the magnetic field is also lower. This leads to a lower synchrotron loss rate and hence to a higher maximum energy of the particles. However, for wide opening angles, the density of cold protons is lower, and the spectrum of produced secondary particles is lower. These effects can be seen in Figs. 9 and 11, where the weighted fluxes for $\xi = 5°$ are lower and more slowly decreasing with energy than those for $\xi = 1.5°$.

It can also be noted from these plots that, for $R_c = 10^{11}$ cm, $\xi = 1.5°$, and a duty cycle of 10%, the expected integrated neutrino signal above 1 TeV from jet-clump interactions will make

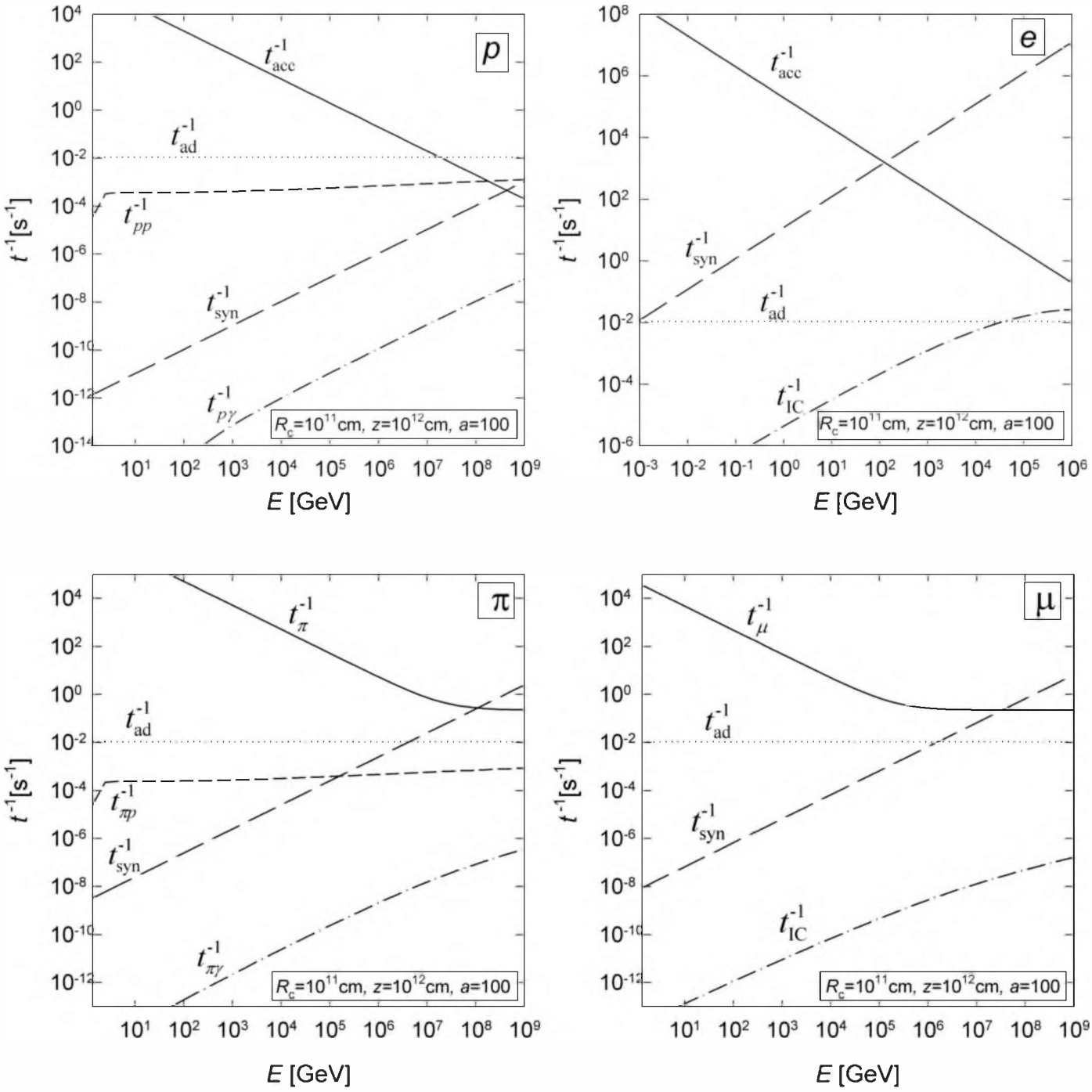

Fig. 10. Proton and electron accelerating and cooling rates (*top panels*), and pion and muon cooling rates (*bottom panels*), for jet-clump interactions at $z = 10^{12}$ cm. Plots shown: accelerating rate (solid lines, *top panels*), decay plus escape rate (solid lines, *bottom panels*), adiabatic cooling rates (dotted lines), synchrotron cooling rates (dashed lines), pp cooling rate (short-dashed line, *top left panel*), πp cooling rate (short-dashed line, *bottom left panel*), $p\gamma$ cooling rate (dash-dotted line, *top left panel*), $\pi\gamma$ cooling rate (dash-dotted line, *bottom left panel*), IC cooling rate (dash-dotted line, *right panels*).

the neutrino output dominate the production at the base of the jet. In the case of low-mass microquasars; however, only the latter will be present (Romero & Vila 2008).

7. Summary

We have studied the effects caused by the magnetic field on the secondary pions and muons that could be produced in microquasar jets. First, assuming an equipartition magnetic field, we calculated the neutrino production at the base of the jet adopting the one-zone approximation. In this case, protons and electrons are shock-accelerated in a localized region near the compact object. A fraction $q_{\rm rel} \sim 0.1$ of the kinetic power of the jet is transferred there to relativistic particles. The energetic protons cool mainly by adiabatic expansion, pp and synchrotron radiation. Hot electrons cool mainly by synchrotron radiation. Secondary pions can be produced through pp and $p\gamma$ interactions, where the targets are the cold protons and the synchrotron photons in the

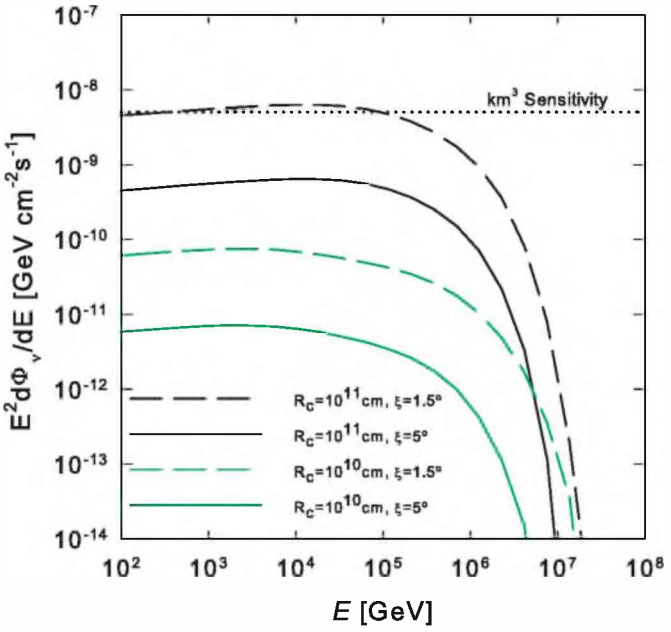

Fig. 11. Differential neutrino fluxes weighted by the squared energy. The solid lines correspond to $\xi = 5°$ and the dashed ones to $\xi = 1.5°$. The black lines correspond to $R_c = 10^{11}$cm and the green lines to $R_c = 10^{10}$ cm.

jet. The pions produced also lose energy by adiabatic expansion, and mainly through synchrotron radiation. Pions still decay giving muons and neutrinos, but with an attenuated spectrum at high energies, due to the effect of pion synchrotron losses. Muons also cool significantly before decaying, giving a much lower neutrino contribution than what was expected from previous, simpler calculations.

Finally, we discussed the case of neutrino production through jet-wind interactions in high-mass microquasars with clumpy stellar winds. The clumps can successfully interact with the jet at large distances from the compact object ($z \gtrsim 5 \times 10^{11}$ cm), where the magnetic field is much weaker than at the jet base. We applied a very simple model adopting the one-zone approximation at different distances along the jet where the clumps can interact. The size of the acceleration region is taken as the radius of the clumps $R_c \approx 10^{10}$–10^{11} cm, and a duty cycle of 10% is assumed. The produced pions and muons in this case do not undergo significant cooling because the magnetic field is relatively low. Hence, the neutrino spectrum obtained is not modified by synchrotron radiation of the secondaries at large distances from the compact object.

As a conclusion, we find that the main contribution to the neutrino emission stems from pp interactions. Pions and muons produced in the vicinity of the compact object are strongly affected by synchrotron losses, and their spectra are attenuated at high energies. As a consequence of that, we find that the neutrino flux is much less than expected when these effects are not taken into account. An additional neutrino contribution, arising from jet-wind interactions in high-mass microquasars, is not affected by these magnetic effects. Still, the detection of a neutrino signal from microquasars seems difficult, but not impossible with next-generation neutrino telescopes such as IceCube, depending on the specific parameters of the system.

The simple models presented here serve to illustrate these effects, which are crucial for assessing the detectability of a neutrino signal from this type of sources. A more realistic treatment including the convection of particles in the jets and a consistent description of the acceleration mechanism will be presented elsewhere.

Acknowledgements. We are very grateful to Gabriela S. Vila for fruitful discussions on the topics of this paper. We also thank Prof. Hugo R. Christiansen for useful comments on the particle injection. M. M. R. is supported by CONICET, Argentina and Universidad Nacional de Mar del Plata (Argentina). G. E. R. is supported by the Argentine agencies CONICET (PIP 452 5375) and ANPCyT (PICT 03-13291 BID 1728/OC-AR). G. E. R. is also supported by the Ministerio de Educación y Ciencia (Spain) under grant AYA 2007-68034-C03-01, FEDER funds.

References

Aharonian, F. A., Akhperjanian, A. G., Aye, K.-M., et al. (HESS Collaboration), 2005, Science, 309, 746
Aiello, S., Ambriola, M., Ameli, F., et al. 2007, Astropart. Phys., 28, 1
Albert, J., Aliu, E., Anderhub, H., et al. (MAGIC Collaboration), 2006, Science, 312, 1771
Albert, J., Aliu, E., Anderhub, H., et al. (MAGIC Collaboration), 2007, ApJ, 665, L51
Atoyan, A. M., & Dermer, C. D. 2003, ApJ, 586, 79
Begelman, M. C., Rudak, B., & Sikora, M. 1990, ApJ, 362, 38
Blumenthal, G. R., & Gould, R. J. 1970, Rev. Mod. Phys., 42, 237
Bosch-Ramon, V., Romero, G. E., & Paredes, J. M. 2006, A&A, 447, 263
Christiansen, H. R., Orellana, M., & Romero, G. E. 2006 Phys. Rev. D, 73, 063012
Falcke, H., & Biermann, P. 1995, A&A, 293, 665
Gaisser, T. K. 1990, Cosmic Rays and Particle Physics (Cambridge: University Press, Cambridge)
Ghisellini, G., Maraschi, L., & Treves, A. 1985, A&A, 146, 204
Halzen, F. 2006, Eur. Phys. J., C46, 669
Heinz, S. 2006, ApJ., 636, 316
Kelner, S. R., & Aharonian, F. A. 2008, Phys. Rev. D, 78, 034013
Kelner, S. R., Aharonian, F. A., & Bugayov, V. V. 2006, Phys. Rev. D, 74, 034018
Khangulyan, D., Hnatic, S., Aharonian, F. A., & Bogovalov, S. 2007, MNRAS, 380, 320
Kording, E. G., Fender, R. P., & Migliari, S. 2006, MNRAS, 369, 1451
Lipari, P., Lusignoli, M., & Meloni, D. 2007, Phys. Rev. D, 75, 123005
Reynoso, M. M., Romero, G. E., & Christiansen, H. R. 2008, MNRAS, 387, 1745
Romero, G. E., Torres, D. F., Kaufman Bernadó, M. M., & Mirabel, I. F. 2003, A&A, 410, L1
Romero, G. E., Owocki, S. P., Araudo, A. T., Townsend, R. H. D., & Benaglia, P. 2007, in Clumping in Hot Star Winds, ed. W. R. Hamann, A. Feldmeier, & L. M. Oskinova, Potsdam, Univ. Verl., 2008, 191
Romero, G. E., & Vila, G. S. 2008, A&A, 485, 623
Waxman, E., & Levinson, A. 2001, Phys. Rev. Lett., 87, 171101